Surface Science 612 (2013) 16–23

Contents lists available at SciVerse ScienceDirect

Surface Science

journal homepage: www.elsevier.com/locate/susc

Surface effects on the structure and lithium behavior in lithiated silicon: A first principles study

Chia-Yun Chou [a], Gyeong S. Hwang [a,b,*]

[a] Materials Science and Engineering Program, University of Texas at Austin, USA
[b] Department of Chemical Engineering, University of Texas at Austin, Austin, TX 78712, USA

ARTICLE INFO

Article history:
Received 13 November 2012
Accepted 13 February 2013
Available online 19 February 2013

Keywords:
Silicon lithiation
Surface effect
Lithium mobility
Density functional theory
ab initio molecular dynamics

ABSTRACT

Silicon anodes with excellent capacity retention and rate capability have been demonstrated utilizing nanoengineered structures, such as nanowires and nanoscale thin films. Here, we present a comparative study using density functional theory calculations to examine the surface effects on the composition, structural evolution, energetics and Li-ion mobility in amorphous Li_xSi alloys ($0.42 \le x \le 3.57$). When the Li content is sufficiently low, our calculations predict a slight Li surface enrichment as the presence of Li atoms contributes to the stabilization of the surfaces. As the Li content is further increased, the near-surface structure and alloy composition become similar to that in the bulk, except for the reduction in Si–Si connectivity within the outermost surface layer. The surface effects tend to be very shallow and only extend to the first couple of atomic layers; nonetheless, our ab initio molecular dynamics simulations highlight the improved Li mobility in the near-surface region. Additionally, our calculations show that Li mobility is extremely sensitive to the alloy composition, and Li diffusivity is enhanced by orders of magnitude in the highly lithiated stage.

1. Introduction

Silicon (Si) has recently emerged as an attractive anode material for lithium-ion (Li-ion) batteries because of its impressive energy-storage capacity. Among all the potential anode materials, Si has the highest known theoretical capacity which is one order of magnitude larger than that of graphite (the most commonly used anode material in today's Li-ion batteries) [1–5]. However, the practical use of Si as an anode material is hampered by its large volume expansion (>300%) [6–8], causing pulverization, loss of electrical contact and consequently early capacity fading. Considerable efforts have been made to overcome this drawback, including alloying Si with active/inactive elements such as tin [9,10] and transition metals [11–14], and structural modifications such as utilizing amorphous phases [15,16], nanoparticles [17,18] and nanowires (NWs) [19].

In general, Si nanostructures can accommodate larger strain and provide better mechanical integrity because their dimensions would limit the size and propagation of cracks, which typically initiate the fracture process [20–23]. Earlier studies not only highlighted the excellent capacity retention of Si NWs [19,24] and thin films [23,25], but also showed easier Li diffusion in the surface region than inside the bulk, leading to faster charge rates. Cui and co-workers [19] have reported Si NWs exhibiting 3193 mAh/g discharge capacity after 10 cycles at C/20 rate (discharge in 20 h) and stable capacity (~3500 mAh/g) up to 20 cycles at C/5 rate. Although the lengths of Si NWs increase and their volume changes appear to be about 400% after lithiation, NWs remain continuous without fractures. Similarly, Si thin films have consistently realized capacities above 2000 mAh/g; Kumta and co-workers [25] have presented amorphous 250 nm-thick Si films with reversible capacities of about 3500 mAh/g at C/2.5 rate for 30 cycles with no obvious signs of failure. While nanostructured Si exhibits many beneficial properties as an anode material, the large surface area may also cause more significant solid electrolyte interphase (SEI) formation and consequently larger capacity loss [26–29].

Recently there is an increasing number of studies employing first principles calculations to investigate lithiation of both crystalline and amorphous Si [30–33]. To study Li behavior at the onset of lithiation, researchers also looked at single Li insertion into Si NWs with different axis orientations and sizes [34,35]. It was shown that surface sites are energetically the most favorable insertion positions, and the diffusion barrier is smaller compared to that in the bulk; in other words, an accelerated Li diffusion can be promoted by shrinking the size of the nanocrystal. However, as the Li content increases, it is practical to look at the alloy formation and Li behavior in amorphous silicon–lithium alloys (*a*-Li–Si) as they are commonly observed during room-temperature lithiation (solid state amorphization) [36]. To the best of our knowledge, there have not been atomistic level studies to specifically address the alloying and structural properties of lithiated Si (*a*-Li–Si) in the near-surface region.

In this work, we use density functional theory (DFT)-based ab initio molecular dynamics (AIMD) to determine the near-surface structures for *a*-Li_xSi alloys of various Li contents ($0.42 \le x \le 3.57$). The structural

* Corresponding author at: Department of Chemical Engineering, University of Texas at Austin, Austin, Texas 78712, USA. Tel./fax: +1 512 471 7060.
E-mail address: gshwang@che.utexas.edu (G.S. Hwang).

0039-6028/$ – see front matter © 2013 Elsevier B.V. All rights reserved.
http://dx.doi.org/10.1016/j.susc.2013.02.004

evolution and energetics in the near-surface region of the alloys are compared with those in the bulk. In particular, we discuss the surface atomic composition and Si–Si coordination along the direction perpendicular to the surface to demonstrate the surface effects on the structure arrangement and incorporation of Li. In addition, AIMD simulations are performed to access the surface effects on the mobility of Li atoms in *a*-Li–Si alloys. The fundamental findings from this theoretical work should provide some insight into the surface effects on the lithiation and delithiation processes of nanostructured Si, while complementing existing experimental observations and also contributing to a better understanding of the lithiation mechanism of Si-based nanomaterials.

2. Computational methods

Quantum mechanical calculations reported herein were performed on the basis of DFT within the generalized gradient approximation (GGA-PW91) [37], as implemented in the Vienna Ab-initio Simulation Package (VASP) [38–40]. Spin polarization of the Li–Si system was also examined, but appears to be insignificant. The projector augmented wave (PAW) method with a planewave basis set was employed to describe the interaction between ion cores and valence electrons. The PAW method is, in principle, an all-electron frozen-core approach that considers exact valence wave functions. Valence configurations employed are: $1s^2 2s^1$ for Li and $3s^2 3p^2$ for Si. An energy cutoff of 350 eV was applied for the planewave expansion of the electronic eigenfunctions. During geometry optimization, all atoms were fully relaxed using the conjugate gradient method until residual forces on constituent atoms become smaller than 5×10^{-2} eV/Å.

The model structures for bulk *a*-Li–Si alloys were created using AIMD simulations (see Refs. [41] and [42] for detailed computational methods). The *a*-Li–Si structures considered are summarized in Table 1; three different supercells were constructed for each alloy composition. The initial slab models were prepared by introducing a 15-Å-thick vacuum gap into the *a*-Li–Si bulk alloys in the *z* direction (for each alloy composition, three different slab models were prepared based on their corresponding bulk structures). To simulate a laterally extended surface in the *x* and *y* directions, we employed the repeated-slab approach by applying periodic boundary conditions to the unit cell in all dimensions as illustrated in Fig. 1. The thinner slab (slab A) contains 64 atoms while the thicker slab (slab B) containing 128 atoms was prepared by stacking two identical 64-atom bulk models in the *z* direction. The slab models were then annealed at 800 K for 4 ps and 300 K for 1 ps to allow sufficient atomic redistribution and relaxation, followed by static energy minimization of the alloy structures. For Brillouin zone sampling, a $(2\times2\times2)$ *k*-point mesh in the scheme of Monkhorst–Pack [43] was used for all bulk amorphous samples summarized in Table 1, and for the corresponding slab models, a $(2\times2\times1)$ *k*-point mesh was used. We carefully checked the convergence of atomic configurations and relative energies with respect to calculation conditions including planewave cutoff energy and *k*-point mesh size.

Table 1
Compositions and optimized supercell volumes of the *a*-Li_xSi alloys examined in this work.

x in *a*-Li_xSi	#Li/#Si	Volume (Å^3/Si)
0.42	19/45	24.5
1.00	32/32	32.9
1.29	36/28	37.8
1.67	40/24	43.3
2.05	43/21	49.6
2.56	46/18	58.2
3.00	48/16	65.2
3.57	50/14	74.8

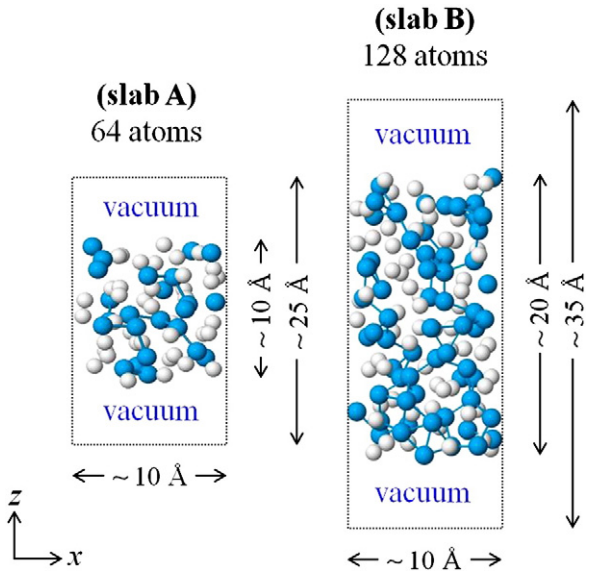

Fig. 1. Side view of *a*-Li–Si slab systems containing 64 atoms (slab A) and 128 atoms (slab B); *x* and *y* dimensions are approximately equal. The white and blue (dark grey) balls represent Li and Si atoms, respectively. The laterally extended surface in the *x* and *y* directions is simulated using the repeated slab approach with a vacuum layer inserted in the *z* direction.

3. Results and discussion

3.1. Surface effect on alloy composition and structure

3.1.1. Surface composition

We examined the variations in Li concentration within the outermost layers of slabs A and B, in comparison with the corresponding bulk counterparts. In Fig. 2, the dashed line with unit slope marks the surface Li concentration being identical to that in the bulk. Here, as also illustrated in Fig. 2 (left panel), we chose the outermost surface layer to be composed of atoms whose surface-projected coordinates have no overlap with other atoms near the surface [44]; the

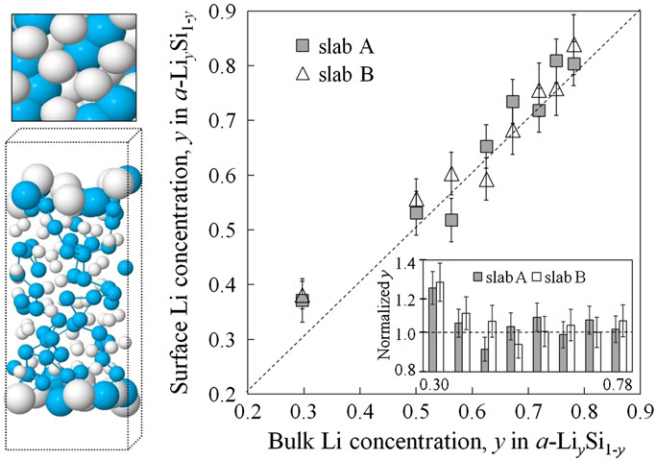

Fig. 2. Comparison between the surface and bulk Li concentrations (*y* in *a*-Li_ySi_{1-y}). The surface composition was obtained by averaging over the top and bottom surfaces (as illustrated in the left panel) of three independent slabs. The white and blue (dark grey) balls represent Li and Si atoms respectively, and the surface atoms are larger in size than that in the bulk. The dash line of slope = 1 marks the surface Li concentration being identical to that in the bulk. The inset shows the normalized surface Li concentrations (with respect to the corresponding bulk values).

overlap radius (=1.8 Å) was based on the projection of the typical Si–Si bond length (≈2.5 Å) [41].

The surface composition analysis shown in Fig. 2 demonstrates two intriguing features. First, the Li contents at the surfaces (of both slabs A and B) generally match well to the corresponding bulk concentrations, particularly when the Li content is relatively high ($y>0.50$ in a-Li_ySi_{1-y}). This indicates that the mixing between Li and Si atoms is homogenous in the bulk as well as near the surfaces, which indubitably coincides with our previous prediction that Li^+ ions are uniformly dispersed in the Si matrix due to their repulsive interactions [41,45]. Second, there is the tendency of slight Li enrichment at the surfaces when the Li content is sufficiently low ($y=0.30$), as demonstrated by the histogram (the inset of Fig. 2) for the normalized surface Li contents with respect to the corresponding bulk concentrations; this is consistent with previous theoretical studies suggesting surface Li enrichment close to the onset of lithiation [33]. The driving force for such phenomenon (which tends to be more pronounced as the Li content gets smaller) could be partly attributed to the surface stabilizing effect of Li atoms, as discussed below.

Looking at the relative stability between the surface and bulk regions of a-Si, the disrupted surface layer may contain a much larger number of strained bonds and coordination defects (such as dangling and floating bonds), compared to the well-relaxed bulk structure. This is clearly demonstrated by the electron density of states (DOS) analysis. As shown in Fig. 3(a), the high concentration of coordination defects (mostly threefold-coordinated Si atoms) gives rise to creation of a large amount of defect states within the gap between the valence band and the conduction band, and also the significant lattice distortions cause the band tails to increase. As a result, the energy gap nearly disappears, as opposed to the occurrence of a sizable band gap in bulk a-Si (which has a nearly perfect tetrahedral network) [Fig. 3(b)]. Note that the predicted gap value of 0.9 eV for bulk a-Si is much smaller than the experimental value of 1.7–1.8 eV [46,47], which is associated with the well-known "band gap problem" of conventional DFT methods (which underestimate semiconductor band gaps typically by a factor of 2 [48]). Given the fact that the surface layer is less stable in comparison to the bulk, Li incorporation in the surface layer should be energetically more favorable (while it could also contribute to stabilizing the a-Si surface).

To quantitatively understand the surface effect on Li incorporation, we also calculated the binding energy (E_b) of a single Li atom at different distances from the surface. Here, E_b is given by:

$$E_b = E_{Li} + E_{Si} - E_{Li+Si} \quad (1)$$

where E_{Li} and E_{Si} are the total energies of single Li atom and a-Si slab, respectively, and E_{Li+Si} is the total energy of Li-inserted a-Si slab. As shown in Fig. 4, although the data points are scattered due to the amorphous nature, a general trend can be observed that E_b gradually becomes larger approaching the surface (smaller z value). This result clearly confirms that Li atoms are more favorably incorporated into the surface region than the bulk region, consistent with previous theoretical studies [34]. However, as discussed earlier, the preferential surface enrichment of Li is only seen when the Li content is sufficiently low, because of the Coulomb repulsion between positively ionized Li atoms (which increases with Li content, and thus limits the favorable accumulation of Li atoms in the surface region).

3.1.2. Configurational evolution and charge state

Fig. 5 shows the bulk and near-surface configurations for a-Li_xSi alloys ($x=0.42$, 1.00, 1.67, and 3.57). At first glance, the bulk and slab systems tend to share similar structural features. Upon alloying with Li, the tetrahedrally bonded Si network is weakened and undergoes disintegration into low-connectivity clusters due to the excess charge transferred from Li [41]. Various shapes of Si network are found at different stages of lithiation, such as rings, strings, dimers, and isolated Si monomers [41].

The connectivity of Si changes following the $(8-N)$ octet rule (or Zintl rule) [49]. If every Li atom donates its 2s electron to Si, the charge transfer in Li_xSi is represented as $(Li^+)_x Si^{x-}$; in the case of $x<4$, $(4-x)$ Si–Si bonds per Si atom are formed to satisfy the $(8-N)$ rule. Such relation between the Si–Si coordination and the charge state is well supported by the result of grid-based Bader charge analysis [50]; the charge states of Si and Li in a-Li_xSi alloys of selected compositions were calculated (with special care to ensure convergence with respect to the grid size). For both the bulk and slab systems, as the Li content increases from $x=0.42$ to 3.57, the Si charge state significantly varies from −0.32 to −3.20 depending on the shape of the Si-network, while the Li charge state remains nearly unchanged around +0.80 to +0.85 (Table 2). At low to moderate Li contents ($x=0.42$ to 1.00), Si_5–Si_8 rings and strings are prevailing. As the Li content is further increased ($x=3.57$), the Si-network loses its connectivity rapidly and only Si_2 dimers and Si monomers remain with charge states estimated to be around −2.3 and −3.2, respectively. It is worthwhile to note that only a partial charge (~0.80e) is transferred from Li to Si, which may indicate that the Si–Li bond is not perfectly ionic; this is reasonable considering that their electronegativity difference is not substantial (electronegativity=1.0 for Li and 1.8 for Si).

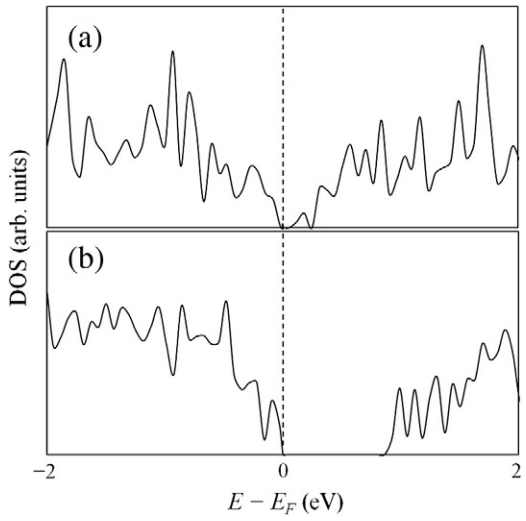

Fig. 3. Total density of states (DOS) of a-Si surface [(a)] and bulk [(b)]. The vertical dashed line indicates the Fermi level (E_F) position.

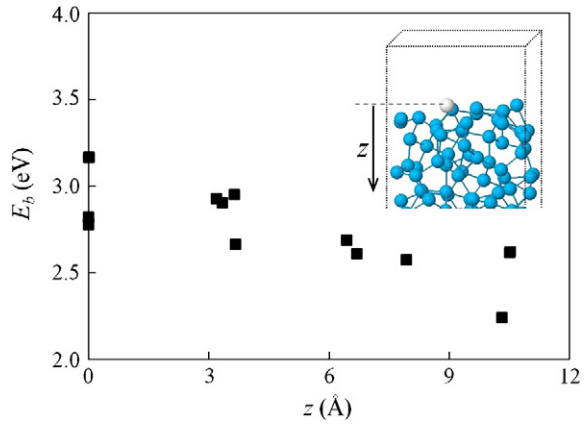

Fig. 4. Variations in Li binding energy (E_b) as a function of distance to the surface (z). The white and blue (dark grey) balls represent Li and Si atoms, respectively.

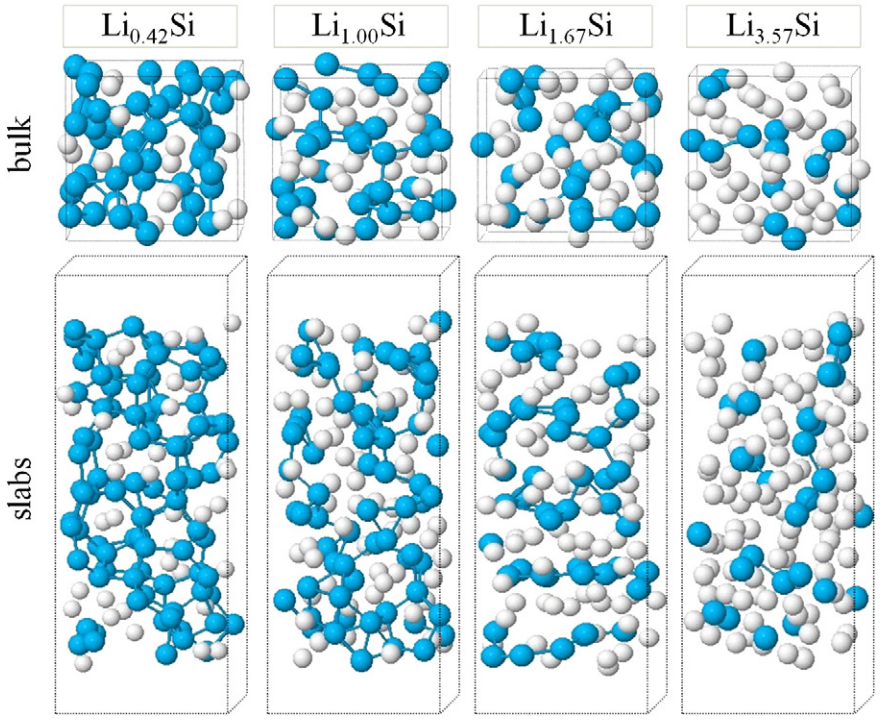

Fig. 5. Atomic structures of the *a*-Li_xSi bulk (top panel) and slab (bottom panel) systems. The white and blue (dark grey) balls represent Li and Si atoms, respectively.

Next, a more detailed structural investigation was conducted to assess the variations in Si–Si connectivity along the direction perpendicular to the surface. Each slab is divided into the outermost surface, subsurface, and center layers as indicated by surf, sub, and center, respectively, in Fig. 6 (the outermost layer is chosen the same way as in the surface composition analysis; below this layer, the slab is divided into sub and center layers of equal thickness in *z*-direction). The Si–Si coordination number (CN_{Si-Si}) is averaged based on the values obtained from the corresponding upper and lower layers of three different slab models as illustrated in Fig. 6 (left panel). The calculated CN_{Si-Si} in different slab layers is then compared with the corresponding bulk value in the histogram shown in Fig. 6. For *a*-$Li_{0.42}Si$, CN_{Si-Si} approximately equals to 3.5 for the bulk system. In the slab system, CN_{Si-Si} noticeably drops to 2.9 in the outermost surface layer while the bulk-like connectivity ($CN_{Si-Si} \approx 3.5$) maintains throughout the subsurface and center layers. In *a*-$Li_{1.67}Si$, CN_{Si-Si} is slightly smaller (≈ 1.7) in the surface layer, below which CN_{Si-Si} is bulk-like (≈ 2.1). The same trend is actually observed for other Li contents, except for highly lithiated phases in which Si atoms mainly exist as dimers and monomers (such that it may not be as meaningful to examine the variations of CN_{Si-Si}). The results clearly demonstrate that the connectivity of surface Si atoms is consistently lower than their bulk counterparts; although the surface effect seems unlikely to extend beyond the outermost surface layer.

Table 2
Calculated Bader charges of Si and Li atoms in selected *a*-Li_xSi bulk and slab systems using a grid based method.

Amorphous		$Li_{0.42}Si$	$Li_{1.00}Si$	$Li_{3.57}Si$
Si	Bulk	$-0.35^{(R)}$	$-0.81^{(R)}$	$-3.20^{(M)}$
			$-0.81^{(S)}$	$-2.20^{(D)}$
	Slab	$-0.32^{(R)}$	$-0.73^{(R)}$	$-3.18^{(M)}$
			$-0.76^{(S)}$	$-2.37^{(D)}$
				$-2.17^{(S)}$
Li		+0.85	+0.84	+0.80

Ring (R), string (S), dimer (D), and monomer (M).

3.2. Near-surface alloying and surface energetics

We looked at how the presence of flat surfaces affects the intermixing between Li and Si atoms, with comparison to that in the bulk. The relative stabilities of *a*-Li_ySi_{1-y} alloys were evaluated by calculating their mixing enthalpies (ΔE_{mix}) with respect to crystalline Si (*c*-Si) and body-centered cubic Li (*bcc*-Li); for each alloy composition, the ΔE_{mix} value was averaged based on three different samples. Fig. 7 shows the variations in ΔE_{mix} for the bulk and slab systems considered; note that slabs A and B have different thicknesses (see Fig. 1). Here, ΔE_{mix} per atom is given by:

$$\Delta E_{mix} = E_{Li_ySi_{1-y}}/N - yE_{Li} - (1-y)E_{Si} \quad (2)$$

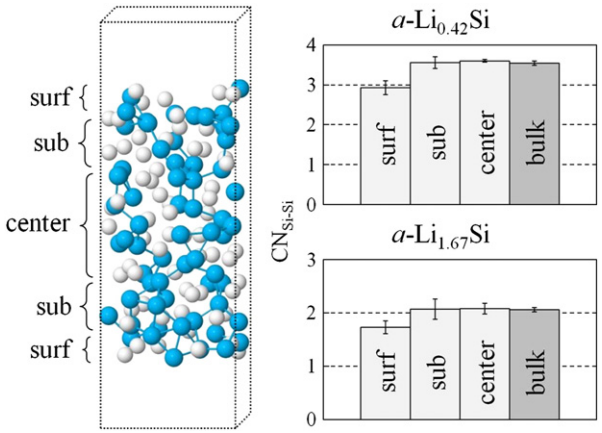

Fig. 6. Side view of a sample *a*-Li–Si slab (left panel); the white and blue (dark grey) balls represent Li and Si atoms, respectively. The histograms (right panel) show variations in Si–Si coordination along the direction perpendicular to the surfaces of *a*-$Li_{0.42}Si$ and *a*-$Li_{1.67}Si$ slabs.

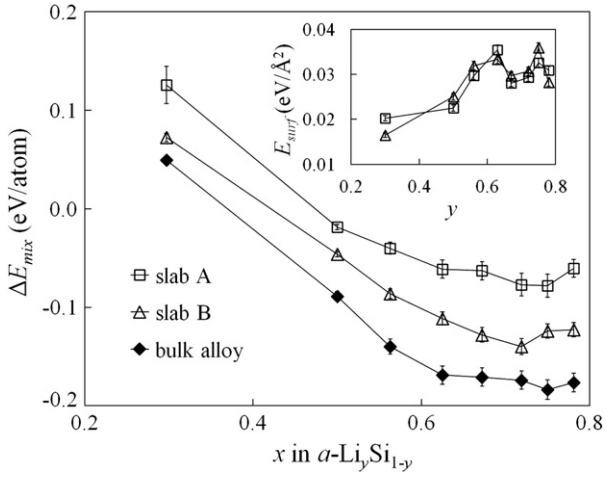

Fig. 7. Variations in mixing enthalpies (ΔE_{mix}) of a-Li$_y$Si$_{1-y}$ alloy for the bulk and slab systems as a function of Li content (y). The calculated surface energies for slabs A and B as a function of Li content are also shown in the inset. For comparison, E_{surf} of a-Si was calculated to be 0.07 eV/Å^2.

where $E_{Li_ySi_{1-y}}$ is the total energy of a lithiated configuration (slab or bulk alloys), y is the atomic fraction of Li, N is the total numbers of Li + Si atoms in the supercell, and E_{Li} and E_{Si} are the per-atom energies of *bcc*-Li and *c*-Si, respectively.

For the bulk system, ΔE_{mix} is initially positive in value, and as the Li content increases, this value drops and changes from positive to negative around 40 at.% Li, and falls to a valley plateau between 60 and 80 at.% Li. The positive value of ΔE_{mix} may suggest the presence of an initial barrier for Li incorporation into the *c*-Si matrix while the negative ΔE_{mix} (above 40 at.% Li) indicates that the alloy formation between Li and Si atoms is energetically favorable.

For the slab systems, the ΔE_{mix} profiles follow the same trend as seen in the bulk case, except for the slight up-shifts in energy, which is apparently associated with the energy cost of creating surfaces. As the slab thickness decreases, the surface contribution becomes more prominent, causing the ΔE_{mix} profile to shift up farther. Based on the energy differences, the surface energy (E_{surf}) per unit area can be calculated by:

$$E_{surf} = (E_{slab} - N_S E_{bulk})/(2A) \quad (3)$$

where E_{slab} is the total energy of the slab, E_{bulk} is the per-atom energy in the bulk, and N_S is the number of atoms in the slab. Here, A is the projected surface area (or slab cross-sectional area) because the slab surfaces are uneven due to the amorphous nature. For different Li contents, the calculated E_{surf} values for slabs A and B are shown in the inset of Fig. 7.

For $y = 0.30$ (in a-Li$_y$Si$_{1-y}$), E_{surf} is predicted to be about 0.02 eV/Å^2 which is substantially smaller than 0.07 eV/Å^2 as estimated for a-Si [51]. The significant reduction in surface energy upon alloying with Li can be explained as follows. The surface energy of a solid can be viewed based on contributions from two parts: (i) surface creation and (ii) surface relaxation and reconstruction [52]. The former reflects the breaking of bonds to make surfaces, and therefore scales approximately with the bond strength of the bulk material. The later reflects the tendency for the surface to relax and reconstruct; when a surface is created, so are unstable dangling bonds (with unpaired valence electrons), which drive the surface atoms to seek a new atomic structure (or bonding configurations) in order to minimize the free energy. The energy cost for creating surfaces in a-Li–Si alloys is expected to be much smaller compared to that for a-Si since the presence of Li is known to significantly weaken the Si – Si bond strength, and in addition, some of covalent Si – Si bonds are replaced with relatively weaker Li – Si bonds (that have substantial ionic character) [41]. Furthermore, as mentioned earlier the unsaturated Si bonds at the surface can be stabilized by Li atoms, and the surface atoms more easily undergo rearrangement and relaxation to reduce the surface energy. Hence, we can expect that the significant drop in E_{surf} (upon alloying Si with Li) is attributed to both the reduced energy cost for surface creation and the increased energy gain via surface relaxation/reconstruction.

Our calculations also show that the E_{surf} value is likely to increase from less than 0.02 to 0.03 eV/Å^2 as y (in a-Li$_y$Si$_{1-y}$) changes from 0.30 to 0.50, and between $y = 0.50$ and 0.78, E_{surf} plateaus around 0.03 eV/Å^2. This slight increase of E_{surf} with y could be to some extent counterintuitive, but may be explained by considering the cationic nature of Li in Si. Note that Li atoms are positively ionized in Si; while in bulk, Li cations are shielded by the surrounding anionic Si network in all directions [41], such screening effect may subside near the surface. As a result, the under screened Coulomb repulsion between Li cations could cause the increase of E_{surf}.

From the calculation results, we can see that the predicted E_{surf} values for slabs A and B are very close to each other regardless of the slab thickness. This suggests that the extent of surface effects is very shallow (consistent with the results of configurational analysis discussed earlier); that is, E_{surf} can converge rapidly with increasing slab thickness, and a 10 Å-thick slab is likely sufficient for characterizing the surface properties of a-Li–Si alloys.

By neglecting the entropy and pressure terms, the free energy of the lithiated configuration can be approximated by the total energy at 0 K, and the formation energy E_f can be obtained by [30,31]

$$E_f = E_{Li_xSi} - (xE_{Li} + E_{Si}) \quad (4)$$

where E_{Li_xSi} is the total energy of the E_{Li_xSi} structure (slab or bulk) divided by the number of Si atoms used in the calculation, x is the number of Li atoms per Si atom, E_{Li} is the total energy of a single *bcc*-Li atom, and E_{Si} is the total energy of a single *c*-Si atom (in the case of lithiated a-Li$_x$Si slabs, E_{Si} denotes the per-atom energy of a 64-atom a-Si surface structure).

The potential (V) of the lithiated a-Li$_x$Si slab and bulk alloys as a function of Li content is obtained from

$$V = -dE_f(x)/dx. \quad (5)$$

Fig. 8(a) shows all the formation energies of the lithiated Li$_x$Si slab and bulk systems, and the corresponding potential-composition curves [Fig. 8(b)] obtained by taking the negative of the derivative of the third order polynomial fittings according to Eq. (5). The voltage curves we derived should be viewed as an approximation since only three configurations were sampled for each composition, and the voltage steps are rather large; nevertheless, our calculations are in a very good agreement with previous simulation and experimental results [16,31]. We see that the voltage curves are not significantly affected by the presence of surfaces, which is in line with the predicted 'shallow surface effect' as the lithiation features are very similar in the bulk and near-surface regions. This result is also consistent with previous studies, which suggest that the lithiation voltage curves are not appreciably influenced by the inclusion of a solid–vacuum interface [33].

3.3. Comparison between bulk and near-surface diffusion

We attempted to examine the surface effects on the mobility of Li atoms in a-Li–Si alloys. AIMD simulations were performed at 800 K to calculate Li diffusivities (D_{Li}) in the slab (slab A) and bulk systems for various a-Li$_x$Si alloys ($x = 1.00$, 1.67, and 3.57). For each alloy, three samples were averaged to calculate the mean-square displacements of Li atoms ($MSD = |R_i(t) - R_i(0)|^2$, where $R_i(t)$ is the position of atom i at time t). From the MSD profiles shown in Fig. 9, D_{Li} values were obtained using the Einstein relation, $D = <MSD>/6t$; the

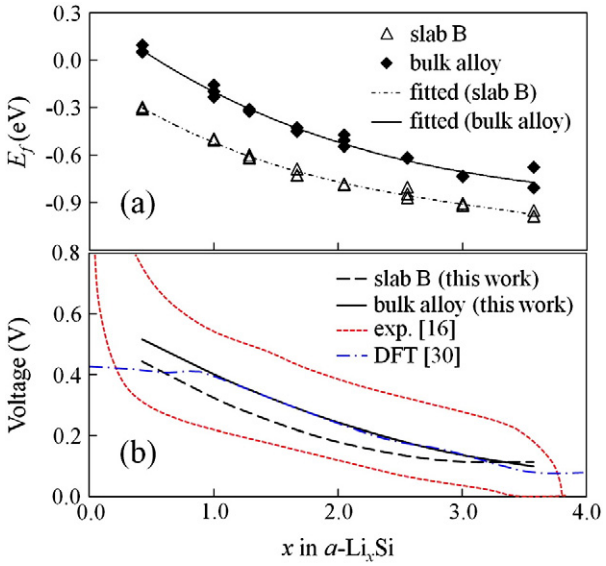

Fig. 8. Formation energy (E_f) [(a)] and potential-composition curves [(b)] obtained from E_f of the a-Li$_x$Si bulk and slab systems. The voltage curves obtained from previous simulation [30] and experimental measurements [16] are also provided for comparison.

angular bracket denotes an averaged value. Here, the MD duration of 7 ps appears to be sufficient to obtain well-converged results; disregarding the first 2 ps, linear fits over a time interval of the following 5 ps yield the D_{Li} values as summarized in the inset of Fig. 9. The mobility of Li is predicted to be enhanced with increasing Li content in both bulk and slab systems; such trend is in line with recent MD simulations, in which D_{Li} was also found to monotonically increase with increasing x in a-Li$_x$Si alloys [53]. More interestingly, we find that D_{Li} values from the slab system are about twice larger than those from the bulk system. The enhanced Li mobility under the influence of surface effects is consistent with previous experiments (demonstrating that the lithiation of Si nanowires proceeds more rapidly in the surface region compared to the center region) [54].

For the highly lithiated a-Li$_{3.57}$Si alloy, additional AIMD simulations were performed to estimate D_{Li} at 600 K and 700 K; the results are summarized in Table 3. Using the calculated D_{Li} values at different temperatures, an *Arrhenius* plot of ln(D_{Li}) versus 1000/T was constructed based on $D = D_0 \exp(-E_a/kT)$, where D_0 is the prefactor, E_a is the activation energy, k is the Boltzmann constant, and T is the

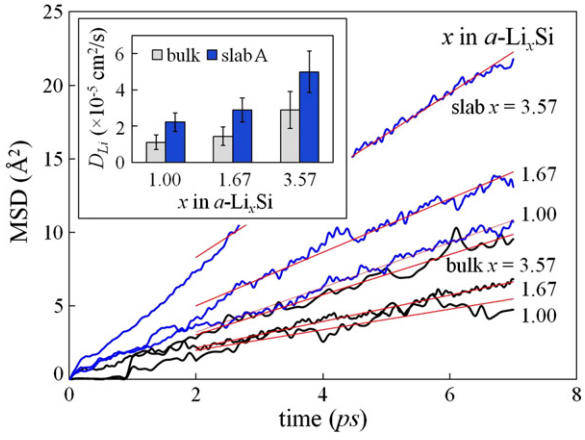

Fig. 9. Variations in the mean square displacements (MSDs) and diffusivities (D_{Li} in the inset) of Li atoms in a-Li$_x$Si bulk and slab systems of various Li contents ($x = 1.00$, 1.67 and 3.57) at 800 K.

Table 3
Predicated Li diffusivities in a-Li$_{3.57}$Si bulk and slab systems at different temperatures as stated.

D_{Li} ($\times 10^{-5}$ cm^2/s)	Bulk	Slab
600 K	0.92 ± 0.24	1.83 ± 0.09
700 K	1.55 ± 0.25	3.39 ± 0.09
800 K	2.50 ± 0.58	4.67 ± 0.47

temperature. From the slope of the *Arrhenius* plot in Fig. 10, E_a for the slab system is estimated to be 0.19 eV which is slightly lower than 0.21 eV for the bulk system. By extrapolating the diffusivity to infinite T, D_0 values are determined to be 8.14×10^{-4} cm^2/s (slab) and 4.92×10^{-4} cm^2/s (bulk), which are comparable to 10^{-3} cm^2/s as predicted within the harmonic approximation to transition state theory, according to which, $D_0 = \nu_0 a^2 \exp(-\Delta S/\kappa)$, assuming ΔS (the entropy difference between the diffusing atom at the saddle point and equilibrium state) is close to zero, ν_0 (the attempt frequency) $\approx 10^{13}$ s^{-1} and a (the distance between adjacent hopping sites) $\approx 10^{-8}$ cm, D_0 would be on the order of 10^{-3} cm^2/s [55]. Taking the predicted E_a and D_0 values, D_{Li} at room temperature is estimated to be around 1.66×10^{-7} (4.32×10^{-7}) cm^2/s in the a-Li$_{3.57}$Si bulk (slab) system (marked by open circles in Fig. 10), which is consistent with the previous calculated values ~10^{-7} cm^2/s in highly lithiated a-Li–Si alloys at room temperature [53]. Although the slabs employed in our calculations are fairly thin, we cannot exclude the contribution from the (bulk-like) subsurface/center regions; hence, the diffusivities calculated here should not be viewed as identical to the pure surface diffusion case. Nevertheless, our results clearly demonstrate that Li diffusion along the surface can be significantly facilitated in comparison to that through the bulk region.

In addition, based on our calculations and D_{Li} values reported in the literature [53,56–62], several observations can be made. First, Li diffusivity in Li–Si alloys at room temperature is a strong function of the Li:Si composition ratio. When the Li concentration is very low (i.e. migration of a single Li atom in bulk c-Si, corresponding to the onset of lithiation), E_a and D_{Li} were obtained to be around 0.60 eV and 2.27×10^{-13} cm^2/s, respectively, from previous DFT-GGA calculations [45]. However, in the highly lithiated a-Li$_{3.57}$Si, the Li diffusivity can increase by several orders of magnitude to $D_{Li} = 1.66\times10^{-7}$ cm^2/s (with $E_a = 0.21$ eV) as presented above. This suggests that D_{Li} can vary by orders of magnitude depending on the stages of lithiation, as also

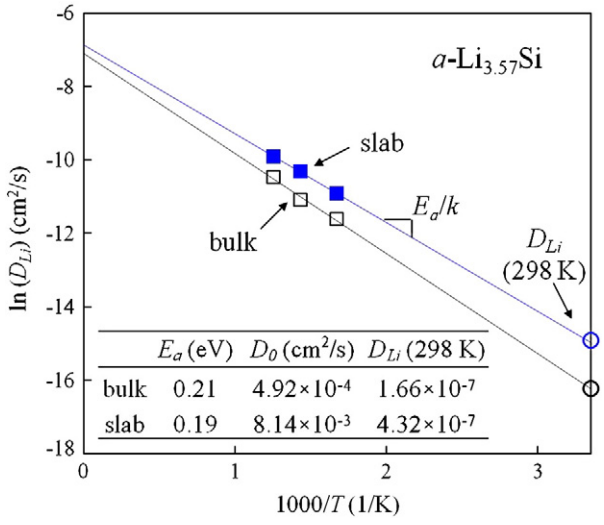

Fig. 10. Arrhenius plot based on the predicated D_{Li} values in a-Li$_{3.57}$Si bulk and slab systems at 600 K, 700 K, and 800 K. The estimated activation barrier, prefactor, and room-temperature diffusivity values (in cm^2/s) are summarized in the inset.

demonstrated by recent MD simulations with an embedded atom method interatomic potential [53]. Second, across lithiated Li_xSi alloys, D_{Li} in amorphous phases can be orders of magnitude larger than that in the corresponding crystalline intermediates [53].

We also noticed that there seem to be discrepancies between calculated and measured Li diffusivities at room temperature. First, the calculated D_{Li} values ($\sim 10^{-7}$ cm^2/s) in lithiated Si at room temperature are orders of magnitude higher than the experimental values ($\sim 10^{-12}$ cm^2/s) [56]. Second, while D_{Li} is predicted to increase monotonically with increasing Li content in a-Li_xSi alloys, earlier experiments reported a 'W' shape with two minimum around $x = 2.1 \pm 0.2$ and 3.2 ± 0.2 (coincide with crystalline Li_7Si_3 and $Li_{13}Si_4$) [56]. One possible explanation is that unlike the simulated amorphous supercells, experimentally lithiated samples could exhibit a certain degree of inhomogeneity in terms of Li concentration and coexistence of crystalline and amorphous phases. As what our calculations pointing out, D_{Li} is highly sensitive to the alloy composition and atomic environment, the above mentioned factors are expected to influence Li diffusion strongly and thus contribute to the discrepancies. In addition, as experimental measurements are generally subject to sample-to-sample variation and differences in test conditions, the widely scattered D_{Li} values (ranging from 10^{-14} to 10^{-8} cm^2/s as reported in the literature [56–62]) make it difficult to directly compare with calculations. Nevertheless, our calculations can provide valuable insights into understanding the atomistic level factors and their effects on Li diffusion properties in lithiated Si nanostructures.

4. Conclusions

In this study, DFT-GGA calculations were performed to examine the surface effects on the composition, structural evolution, energetics, and Li diffusion properties of a-Li_xSi alloys ($x = 0.42$ to 3.57); the slab model was used to simulate the presence of surfaces. Our simulations predict a slight surface enrichment of Li atoms when the Li content is sufficiently low, which may contribute to stabilizing the alloy surface. With increasing Li content, the Coulomb repulsion between Li cations becomes more pronounced and results in well dispersed Li distribution in the bulk as well as near-surface regions. Detailed structural analysis shows that the slab and bulk systems share very similar structural features; the presence of surfaces tends to only affect the outermost surface layer with the reduced Si–Si connectivity, and below this layer the bulk-like connectivity is restored.

According to our mixing enthalpy calculations, the alloy formation (for bulk and slab systems both) becomes progressively more favorable with increasing Li content while the most stable alloy structure occurs between 60 and 80 at.% Li. As indicative of the shallow surface effect, the calculated surface energy (E_{surf}) converges rapidly with increasing slab thickness. Upon the introduction of Li ($x = 0.42$), E_{surf} decreases substantially from 0.07 eV/Å^2 for a-Si to less than 0.02 eV/Å^2, marking the significant surface stabilization due to the presence of Li atoms. With increasing Li content, the Li^+–Li^+ repulsion grows more apparent and results in higher E_{surf} which reaches a plateau around 0.03 eV/Å^2 between $x = 1.00$ and 3.57.

We also performed AIMD simulations at 800 K to determine Li diffusivities in a few selected systems ($x = 1.00$, 1.67, and 3.57). The results show that the mobility of Li in lithiated Si alloys depends strongly on the Li:Si composition ratio and local atomic environment. The diffusivity of Li atoms increases continuously during lithiation; approximately from 10^{-13} cm^2/s at the onset of lithiation to 10^{-7} cm^2/s in the highly lithiated a-$Li_{3.57}Si$ at room temperature. More importantly our calculations clearly demonstrate that the presence of surfaces facilitates faster Li-ion diffusion, and the D_{Li} values for the slab system are predicted to be about twice larger than those for the bulk. The present study greatly assists in understanding the a-Li–Si alloy formation near the surface, and can also complement existing experimental observations as to the behavior of Li in nanostructured Si alloys, in which the surface effect is prominent.

Acknowledgments

This work was supported by the R.A. Welch Foundation (F-1535). We would like to thank the Texas Advanced Computing Center for use of their computing resources.

References

[1] M. Winter, J.O. Besenhard, Electrochim. Acta 45 (1999) 31.
[2] R.A. Sharma, R.N. Seefurth, J. Electrochem. Soc. 123 (1976) 1763.
[3] B.A. Boukamp, G.C. Lesh, R.A. Huggins, J. Electrochem. Soc. 128 (1981) 725.
[4] M.N. Obrovac, L. Christensen, Electrochem. Solid-State Lett. 5 (2004) A93.
[5] U. Kasavajjula, C. Wang, A.J. Appleby, J. Power Sources 163 (2007) 1003.
[6] M.N. Obrovac, L. Christensen, D.B. Le, J.R. Dahn, J. Electrochem. Soc. 154 (2007) A849.
[7] X.H. Liu, L.Q. Zhang, L. Zhong, Y. Liu, H. Zheng, J.W. Wang, J.-H. Cho, S.A. Dayeh, S.T. Picraux, J.P. Sullivan, S.X. Mao, Z.Z. Ye, J.Y. Huang, Nano Lett. 11 (2011) 2251.
[8] H. Wu, Y. Cui, Nano Today 7 (2012) 414.
[9] L.Y. Beaulieu, K.C. Hewitt, R.L. Turner, A. Bonakdarpour, A.A. Abdo, L. Christensen, K.W. Eberman, L.J. Krause, J.R. Dahn, J. Electrochem. Soc. 150 (2003) A149.
[10] J.-H. Ahn, G.X. Wang, J. Yao, H.K. Liu, S.X. Dou, J. Power Sources 119–121 (2003) 45.
[11] O. Mao, R.L. Turner, I.A. Courtney, B.D. Fredericksen, M.I. Buckett, L.J. Krause, J.R. Dahn, Electrochem. Solid-State Lett. 2 (1999) 3.
[12] M.D. Fleischauer, J.M. Topple, J.R. Dahn, Electrochem. Solid-State Lett. 8 (2005) A137.
[13] L.Y. Beaulieu, T.D. Hatchard, A. Bonakdarpour, M.D. Fleischauer, J.R. Dahn, J. Electrochem. Soc. 150 (2003) A1457.
[14] A. Netz, R.A. Huggins, W. Weppner, J. Power Sources 95 (2003) 119.
[15] S. Bourderau, T. Brousse, D.M. Schleich, J. Power Sources 81–82 (1999) 233.
[16] T.D. Hatchard, J.R. Dahn, J. Electrochem. Soc. 151 (2004) A838.
[17] B. Gao, S. Sinha, L. Fleming, O. Zhou, Adv. Mater. 13 (2001) 816.
[18] J. Graetz, C.C. Ahn, R. Yazami, B. Fultz, Electrochem. Solid-State Lett. 6 (2003) A194.
[19] C.K. Chan, H. Peng, G. Liu, K. McIlwrath, X.F. Zhang, R.A. Huggins, Y. Cui, Nat. Nanotechnol. 3 (2008) 31.
[20] H. Ghassemi, M. Au, N. Chen, P.A. Heiden, R.S. Yassar, ACS Nano. 5 (2011) 7805.
[21] J. Yang, M. Winter, J.O. Besenhard, Solid State Ionics 90 (1996) 281.
[22] R.A. Huggins, W.D. Nix, Ionics 6 (2000) 57.
[23] J. Li, A.K. Dozier, Y. Li, F. Yang, Y.T. Cheng, J. Electrochem. Soc. 158 (2011) A689.
[24] L.F. Cui, R. Ruffo, C.K. Chan, H. Peng, Y. Cui, Nano Lett. 9 (2009) 491.
[25] J.P. Maranchi, A.F. Hepp, P.N. Kumta, Electrochem. Solid-State Lett. 6 (2003) A198.
[26] P. Verma, P. Maire, P. Novák, Electrochim. Acta 55 (2010) 6332.
[27] C.K. Chan, R. Ruffo, S.S. Hong, Y. Cui, J. Power Sources 189 (2009) 1132.
[28] H. Wu, G. Chan, J.W. Choi, I. Ryu, Y. Yao, M.T. McDowell, S.W. Lee, A. Jackson, Y. Yang, L. Hu, Y. Cui, Nat. Nanotechnol. 7 (2012) 310.
[29] X. Wu, Z. Wang, L. Chen, X. Huang, Electrochem. Commun. 5 (2003) 935.
[30] V.L. Chevrier, J.R. Dahn, J. Electrochem. Soc. 157 (2010) A392.
[31] V.L. Chevrier, J.R. Dahn, J. Electrochem. Soc. 156 (2009) A454.
[32] V.L. Chevrier, J.W. Zwanziger, J.R. Dahn, J. Alloys Compd. 496 (2010) 25.
[33] M.K.Y. Chan, C. Wolverton, J.P. Greeley, J. Am. Chem. Soc. 134 (2012) 14362.
[34] Q. Zhang, W. Zhang, W. Wan, Y. Cui, E. Wang, Nano Lett. 10 (2010) 3243.
[35] T.L. Chan, J.R. Chelikowsky, Nano Lett. 10 (2010) 821.
[36] P. Limthongkul, Y.I. Jang, N.J. Dudney, Y.M. Chiang, Acta Mater. 51 (2003) 1103.
[37] P.E. Blochl, Phys. Rev. B 50 (1994) 17953.
[38] G. Kresse, J. Hafner, J. Phys. Rev. B 47 (1993) 558.
[39] G. Kresse, J. Furthmuller, Comput. Mater. Sci. 6 (1996) 15.
[40] G. Kresse, J. Furthmuller, J. Phys. Rev. B 54 (1996) 11169.
[41] H. Kim, C.Y. Chou, J.G. Ekerdt, G.S. Hwang, J. Phys. Chem. C 115 (2011) 2514.
[42] S.-H. Lee, G.S. Hwang, J. Chem. Phys. 127 (2007) 224710.
[43] H.J. Monkhorst, J.D. Pack, Phys. Rev. B 13 (1976) 5188.
[44] S.H. Lee, J.A. Stephens, G.S. Hwang, J. Phys. Chem. C 114 (2010) 3037.
[45] H. Kim, K.E. Kweon, C.Y. Chou, J.G. Ekerdt, G.S. Hwang, J. Phys. Chem. C 114 (2010) 17942.
[46] A.V. Shah, J. Meier, E. Vallat-Sauvain, N. Wyrsch, U. Kroll, C. Droz, U. Graf, Sol. Energy Mater. Sol. Cells 78 (2003) 469.
[47] E. Fefer, Y. Shapira, Appl. Phys. Lett. 67 (1995) 3.
[48] L.J. Sham, M. Schlüter, Phys. Rev. Lett. 51 (1983) 20.
[49] S.M. Kauzlarich, Chemistry, Structure, and Bonding of Zintl Phases and Ions, Wiley-VCH Publishers, New York, 1996.
[50] G. Henkelman, A. Arnaldsson, H. Jonsson, Comput. Mater. Sci. 36 (2006) 354.
[51] S. Hara, S. Izumi, T. Kumagai, S. Sakai, Surf. Sci. 585 (2005) 17.
[52] G.P. Srivastava, Rep. Prog. Phys. 60 (1997) 561.
[53] Z. Cui, F. Gao, Z. Cui, J. Qu, J. Power Sources 207 (2012) 150.
[54] X.H. Liu, H. Zheng, L. Zhong, S. Huang, K. Karki, L.Q. Zhang, Y. Liu, A. Kushima, W.T. Liang, J.W. Wang, J.H. Cho, E. Epstein, S.A. Dayeh, S.T. Picraux, T. Zhu, J. Li, J.P. Jullivan, J. Cumings, C. Wang, S.X. Mao, Z.Z. Ye, S. Zhang, J.Y. Huang, Nano Lett. 11 (2011) 3312.
[55] X.R. Wang, X. Xiao, Z. Zhang, Surf. Sci. 512 (2002) L361.

[56] N. Ding, J. Xu, Y.X. Yao, G. Wegner, X. Fang, C.H. Chen, I. Lieberwirth, Solid State Ionics 180 (2009) 222.
[57] P. Johari, Y. Qi, V.B. Shenoy, Nano Lett. 11 (2011) 5494.
[58] J. Xie, N. Imanishi, T. Zhang, A. Hirano, Y. Takeda, O. Yamamoto, Mater. Chem. Phys. 120 (2010) 421.
[59] N. Balke, S. Jesse, Y. Kim, L. Adamczyk, A. Tselev, I.N. Ivanov, N.J. Dudney, S.V. Kalinin, Nano Lett. 10 (2010) 3420.
[60] E.M. Pell, Phys. Rev. 119 (1960) 1014.
[61] E.M. Pell, Phys. Rev. 119 (1960) 1222.
[62] K. Yoshimura, J. Suzuki, K. Sekine, T. Takamura, J. Power Sources 174 (2007) 653.